

Theoretical investigation of the structural, elastic, electronic, and dielectric properties of alkali-metal-based bismuth ternary chalcogenides

Syam Kumar R^{1,*}, Akinlolu Akande^{1,2}, Fedwa El-Mellouhi^{1,2}, Heesoo Park^{1,2}, and Stefano Sanvito³

¹Department of Health and Nutritional Science, Institute of Technology Sligo, Ash Lane, Co. Sligo, F91 YW50, Ireland

²Qatar Environment and Energy Research Institute, Hamad Bin Khalifa University, P.O. Box 34110, Doha, Qatar

³School of Physics, AMBER and CRANN Institute, Trinity College, Dublin 2, Ireland



(Received 18 December 2019; accepted 11 May 2020; published 10 July 2020)

The past decade has witnessed the rapid introduction of organic-inorganic hybrid compounds in photovoltaic applications. Motivated by the strong demand for stable and nontoxic materials in this class, we report a theoretical study on the structural, elastic, electronic, thermodynamic and dielectric properties of alkali-metal-based bismuth ternary chalcogenides. In particular, we employ state-of-the-art density functional theory to explore the potential of $ABiX_2$ and $ABiX_3$ ($A = Na, K$ and $X = O, S$) as light-absorbing media. All the compounds under investigation are found to be thermodynamically and mechanically stable, with a semiconductor band structure. The Kohn-Sham band gaps range between 0.80 eV and 1.80 eV, when calculated with semilocal functionals, values that increase to 1.24–2.47 eV with hybrid ones. Although all but $NaBiO_2$ and $KBiO_2$ are indirect band-gap semiconductors, the onset of the imaginary part of their dielectric functions, the optical gap, is only marginally larger than the quasiparticle gap. This is due to the generally flat nature of both the conduction and the valence bands. We then expect these compounds to absorb light in the upper part of the visible spectrum. In all cases the valence band is dominated by O-*p* and S-*p* orbitals and the conduction one by Bi-*p*, suggesting the possibility of excitons with low binding energy. The only exceptions are $NaBiO_2$ and $KBiO_2$ for which the O-*p* states dominate the density of states at both sides of the band gap.

DOI: 10.1103/PhysRevMaterials.4.075401

I. INTRODUCTION

The twenty first century has witnessed a rising demand for efficient alternative energy sources to substitute the rapidly depleting fossil fuel reserves and to provide greener and more sustainable solutions to the global energy demand. Solar power is commonly recognized to be the ultimate unlimited energy source, but its harvesting is not free of challenge. The simplest, oldest, and most commonly used solar photovoltaic (PV) device is the silicon solar cell. In fact, silicon in both its mono- and polycrystalline form is still the dominant material in PV technology and takes more than 90% of the market share [1]. Alternative materials platforms for PV, which have already enjoyed some commercial exploitation, include CdTe and $CuIn_xGa_{1-x}Se_2$ (CIGS) thin films [2,3]. All these PV media, unfortunately, share the need for relatively expensive high-temperature processing, which offsets the low cost of the associated raw materials. The second drawback of Si-based PV technology is that Si is generally brittle, so that it can be hardly integrated over the flexible substrates required by some mobile applications (e.g., wearable electronics). For these reasons, significant research has been dedicated to exploring materials solutions alternative to Si. These include III-IV

semiconductors (in particular for multiple-junction tandem cells), dye-sensitized and organic compounds, GaAs-based structures, and intermediate-band-gap solar materials [4–8].

A materials family, which has recently attracted enormous attention, is that of the perovskites, in particular hybrid organic-inorganic perovskites (HOIPs). Discovered in the late 80's [9] and early 90's [10], HOIPs are generally easy to synthesize and show strong light properties [11]. Solar cells made of HOIPs have reached efficiencies exceeding 20% in less than a decade from their discovery [12] and are now considered among the top candidate materials for affordable PV technologies. Among their properties, these compounds are solution processable [13,14] and they can be deposited cheaply by spin coating from solution and by co-evaporation [15–17]. $MAPbI_3$ (MA = methylammonium, CH_3NH_3) is the most celebrated member of this family, having an experimental band gap conveniently placed at the optimum value of the AM1.5G solar illumination spectrum [18] and presenting a high absorption coefficient. This feature allows one to fabricate films thinner than the carrier diffusion length for an optimal carrier-generation profile [7].

Unfortunately, there are also concerns around HOIPs. These are related to their stability in the air, in particular, their fragility against humidity, and the health issues arising from the presence of the toxic element Pb [19]. A number of strategies have been proposed to overcome these limitations. Some of them have an engineering nature, for instance, the attempt to encapsulate $MAPbI_3$ within humidity-protecting layers, but most of the effort has concentrated on synthesising alternative compounds. The replacement of MA with other organic molecules generally tends to reduce the band gap and

*syamkumar.rameshkumar@mail.itsligo.ie

may further compromise the stability [20], while substituting Pb with Sn results in air-unstable compounds because of the ease of oxidation of the Sn^{2+} ion [13,21]. Mixed-cation [20] and double perovskites [22] have also been considered, although tuning their properties is a complex task. All these attempts suggest that surpassing the PV properties of MAPbI_3 is by no means simple. Intriguingly, the unique characteristic of the Pb-based HOIPs is the presence of the Pb $6s^2$ lone pair that causes strong Pb $6s$ -I $5p$ antibonding character of the valence band of the high-symmetry perovskite structure [23].

Bismuth (Bi) is the only element in the period 6 with an outer $6s^2$ lone pair and low toxicity [24]. Bi is also the heaviest group V element and exhibits strong spin-orbit coupling (SOC), which often determines the relevant features of the band structure [25]. Such similarity with Pb makes Bi an attractive element to develop new compounds for PV applications, and in fact, Bi-based ternaries have been recently the subject of both theoretical and experimental work. These include halide-containing materials such as $(\text{MA})_3\text{Bi}_2\text{I}_9$, $\text{Cs}_3\text{Bi}_2\text{I}_9$, BiSI and BiOI , and some chalcogenides, AgBiS_2 [26–29]. Some of the halide-containing compounds, namely $(\text{MA})_3\text{Bi}_2\text{I}_9$, $\text{Cs}_3\text{Bi}_2\text{I}_9$ and $(\text{MA})_3\text{Bi}_2\text{I}_9\text{Cl}_x$, have been tested for light absorption [30–32] but unfortunately only display modest efficiencies ranging between 0.1% and 1%.

An interesting chemical possibility that certainly may improve the materials' structural and the thermodynamic stability is that of replacing the halide anion with a chalcogen element such as O and S. One has then the option to form ternaries with either 1:1:2 or 1:1:3 stoichiometric ratios, whose prototypes are CsBiO_2 and CsBiO_3 , respectively, and where Bi is either in the +3 or +5 oxidation state. Several compounds in this class have been synthesized and experimentally characterized with piezoelectric and photocatalytic applications. For some of them, theoretical work also exists. These include NaBiO_2 [33], KBiO_2 [34], RbBiO_2 [33,34], CsBiO_2 [33], NaBiO_3 [35–38], KBiO_3 [39], NaBiS_2 [40,41], and KBiS_2 [40,41].

In the present work, we explore theoretically the potential of this class of ternary Bi-based chalcogenides for PV applications, by exploring their structural, thermodynamic, mechanical, elastic, electronic, and dielectric properties. For all compounds, the computed optimal crystal structure is found to be consistent with available experimental data. The only exception is for NaBiS_2 and KBiS_2 , which are calculated trigonal instead of cubic as reported in the literature. This difference is attributed to the site occupation disorder in the experimental samples. The theoretical and experimental data can be reconciled by assuming that the experimental structure is the result of a macroscopic average of various equivalent trigonal orientations. All compounds are indirect gap semiconductors with the exception of NaBiO_2 and KBiO_2 .

The paper is organized as follows. Section II discusses the computational methods used for the calculations and our strategy for constructing materials prototypes. In Secs. III A, III B, III C, III D, and III E, we present our results alongside a discussion of the structural, thermodynamic, mechanical, elastic, electronic, and dielectric properties of all compounds, respectively. Finally, in Sec. IV we summarize our finding and highlight possible future directions.

II. METHODS

A. Computational details

Structural optimization and the calculation of the electronic structure and dielectric properties have been performed by density functional theory (DFT) as implemented in the all-electron code FHI-AIMS (Fritz Haber Institute Ab Initio Molecular Simulations) [42]. The Perdew-Burke-Ernzerhof (PBE) [43] parametrization of the generalized gradient approximation (GGA) of the exchange-correlation energy has been used throughout. FHI-AIMS writes the electron density and all the operators over an all-electron numerical-atomic-orbitals basis set, and here we have used the ‘tight’ option, which provides safe pre-constructed default definitions for the different chemical species (elements). The Broyden-Fletcher-Goldfarb-Shanno (BFGS) algorithm [44] has been used to relax both the atomic coordinates and the lattice vectors of all the ternary compounds, with convergence cutoffs of 10^{-3} eV, 10^{-4} eV, and 10^{-3} eV/Å, respectively, for the Kohn-Sham eigenvalues, the total energy, and the atomic forces. The reciprocal space integration has been performed over a $8 \times 8 \times 8$ grid.

In general, the role of van der Waals interactions in solids is still a matter of discussion [45], although in some cases they provide an overall improvement of the cohesive properties of ionic and semiconductor solids [46], and there is evidence that these contribute in determining the structure of HOIPs [47]. The GGA-PBE functional does not describe weak dispersive forces. We remedy this shortfall by including the Tkatchenko-Scheffler van der Waals correction scheme [48], when performing the structural relaxation. Spin-orbit coupling (SOC) is considered in the calculation of the electronic structure.

The linear macroscopic dielectric tensor, $\varepsilon_{ij}(\omega)$, is calculated within the random phase approximation (RPA) framework as reported by Ambrosch-Draxl *et al.* [49]. The frequency-dependent imaginary part of the interband contribution to the linear dielectric tensor is computed with FHI-AIMS as

$$\text{Im}(\varepsilon_{ij}(\omega)) = \frac{1}{\pi\omega^2} \sum_{n,n'} \int_{\vec{k}} p_{i;n',n,\vec{k}} p_{j;n',n,\vec{k}} [f_0(\varepsilon_{n,\vec{k}}) - f_0(\varepsilon_{n',\vec{k}})] \delta(\varepsilon_{n',\vec{k}} - \varepsilon_{n,\vec{k}} - \omega), \quad (1)$$

where $\varepsilon_{n,\vec{k}}$ is the eigenvalue of the Kohn-Sham (KS) eigenstate of band index n and wave vector \vec{k} , $f_0(\varepsilon_{n,\vec{k}})$ is the Fermi function with ε_F being the chemical potential, $\delta(\varepsilon_{n',\vec{k}} - \varepsilon_{n,\vec{k}} - \omega)$ is the Dirac function (approximated as a Gaussian), and $p_{j;n',n,\vec{k}}$ are the momentum matrix elements calculated from the real-space basis functions in k space and the KS-eigenstate basis. The broadening values for the Fermi and Gaussian functions are set as 0.001 eV and 0.02 eV, respectively. The dielectric tensor thus obtained is hermitian and the number of linearly independent components depends on the symmetry of the crystal. By using the Kramers-Kronig transformation, the corresponding real parts can be obtained. Since the calculation of the density of states (DOS) and the dielectric function are very sensitive to the k -point grid, grids as large as $15 \times 15 \times 15$ and $10 \times 10 \times 10$ are used for ABiX_2 and ABiX_3 type compounds, respectively.

Throughout this project we have also used the Vienna *ab initio* simulation package (VASP) [50]. VASP implements DFT within the projector-augmented wave method [51] and it has been utilized for a few test calculations and to compute the elastic constants of the materials under consideration. All VASP calculations are at the PBE-GGA level and the FHI-AIMS optimized structures have been used to compute the elastic constants.

In order to correct the systematic band gap underestimation of the GGA, we have performed calculations using the Gritsenko, van Leeuwen, van Lenthe, and Baerends functional (GLLB) [52], as implemented in the GPAW code [53]. Its optimization for solids (GLLB-SC) [54] has been reported to predict band gaps in good agreement with experiments [55]. The GLLB-SC functional presents a computational cost significantly lower than that of hybrid functionals without compromising on the accuracy [56]. Hence, GLLB-SC has been chosen to correct the band gaps of the Bi chalcogenides investigated here.

Finally, the dynamic stability of some of the prototypes required to be validated. For this purpose, we have carried out phonon band structure calculations using the finite displacement method as implemented in the Phonopy package [57]. In particular, we have used a $2 \times 2 \times 2$ supercell and a $6 \times 6 \times 6$ k -grid mesh.

B. Construction of the prototypes

From our literature survey of Bi-containing ternary compounds, we have decided to focus on the two stoichiometry compositions $ABiX_2$ and $ABiX_3$, where $A = Na, K$ and $X = O, S$. These compositions appear promising to host suitable semiconductors for PV applications, with the finite band gap and robust structural stability. In the case of the oxides, crystallographic data exist for $NaBiO_2$, $NaBiO_3$, and $KBiO_2$. Therefore, their initial structure has been taken from the Materials Project Library [58]. The $2 \times 1 \times 1$ $NaBiO_2$ supercell from the Materials Project Library has been chosen to match the lattice parameters of the experimentally reported structure [33]. In contrast, $KBiO_3$ has been claimed to crystallize in the cubic crystal system with space group $Im\bar{3}$ (No. 204), although no crystallographic data are available. The closest prototype included in the crystallographic database is the one lying in the space group, $Pn\bar{3}$ (No. 201), whose primitive cell contains 60 atoms. Alternatively, one can use the experimental structure of $NaBiO_3$ as a prototype for $KBiO_3$ (30 atoms per cell). By comparing the total energy of the final structures relaxed from these two prototypes, we find the second one to be most stable. Therefore, this is the structure that we investigate further. All these structures have been relaxed with GGA-PBE, including van der Waals corrections. Then, we have replaced in the final structures the O ions with S, so as to generate the prototypes for $NaBiS_3$ and $KBiS_3$. These compounds also have been fully relaxed.

If one employs the same strategy for $NaBiS_2$ and $KBiS_2$, the resulting prototypes will belong to the tetragonal and monoclinic system, respectively. However, it has been reported that there exist for both high-symmetric cubic structures [59], which unfortunately are not available in any of the crystal structure databases. As such, together with the tetragonal

and monoclinic structures, we have also constructed cubic prototypes of $NaBiS_2$ and $KBiS_2$. These are obtained by modifying the rocksalt structure according to the prescription adopted in Ref. [60] for ternary $APnE_2$ compounds ($A = Na, K, Ag$; $Pn = As, Sb, Bi$; $E = S, Se, Te$).

The thermodynamic stability of all compounds investigated has been assessed by computing the convex hull diagrams and the possible decomposition reaction pathways. In this case, we have considered decompositions along with binary phase with the crystal structure of such binaries extracted from the AFLOWLIB.org library [61,62]. Finally, the k -point paths in reciprocal space used to compute the band structure have been obtained by using the *aflow-online* tool [63].

III. RESULTS AND DISCUSSION

We present here the structural, thermodynamic, elastic, mechanical, electronic, and dielectric properties of the two classes of alkali-metal Bi-based ternary chalcogenides, $ABiX_2$ and $ABiX_3$. Here, A is a monovalent Na or K cation and X is the divalent O or S anion, thus that Bi is either in the +3 or +5 oxidation state.

A. Structural properties

The computed cell parameters, lattice system, and space group of the ternary Bi-chalcogenides after relaxation are tabulated in Table I, while their corresponding ball-and-stick structural diagrams are presented in Fig. 1. Let us discuss the oxides first. $NaBiO_2$ is calculated to be a monoclinic crystal with the $C2/c$ space group, consistent with available experiments [33]. The computed lattice constants are in close agreement with crystallographic data, except for the c parameter, which is overestimated (5.97 Å against 5.88 Å) as sometimes expected from the GGA. In $NaBiO_2$, the Bi cations are bonded to four O atoms in a tetrahedral local coordination (see polygons diagrams in Fig. 1). When the lone pair is taken into consideration, Bi could be assigned to a trigonal bipyramidal molecular geometry. In such $C2/c$ structure, Na is found in octahedral coordination. In contrast, $NaBiO_3$, where the Bi oxidation state becomes +5, has a trigonal layered structure and it is found in the much more symmetric $R\bar{3}$ space group. Also in this case, there is good agreement between the computed structural parameters and those available from diffraction experiments [35], with an elongation of the planar lattice constant $a = b$ (5.69 Å against the experimental value of 5.57 Å) and a compression of the out-of-plane one, c (15.44 Å against 15.99 Å). In this case, both the Na and Bi cations have octahedral coordination with O. The Na octahedra bond to each other via edge sharing, and so do the Bi ones. Then, there exist both corner-sharing and face-sharing coordination between the Na and Bi octahedra. In general, this structure appears to be made of BiO_6 octahedra monolayers separated by intercalated Na.

Moving to K-containing oxides, we find that $KBiO_2$ crystallizes in a layered structure of the monoclinic system with $C2/c$ space group. This is also consistent with crystallographic data [64] although we find a rather large deviation between one of the calculated lattice parameters, $c = 6.55$ Å, with respect to its corresponding experimental value (5.97 Å).

TABLE I. Structural parameters of the eight compounds investigated after full structural relaxation. In the table, we report the number of atoms per unit cell N_a , the calculated lattice parameters (a , b , c), the lattice vector angles (α , β , γ), the crystal structure system (CSS), the space group (SG) with the space group number in bracket, the atomization energy ΔE_a , and the decomposition energy ΔE_d .

Compound	N_a	(a, b, c) (Å)			(α, β, γ) (°)			CSS	SG	ΔE_a (eV)	ΔE_d (eV)
		a	b	c	α	β	γ				
NaBiO ₂	16	7.38	7.32	5.97	90.0	127.0	90.0	Monoclinic	$C2/c$ (15)	-4.18	0.29
NaBiO ₃	30	5.69	5.69	15.44	90.0	89.9	119.9	Trigonal	$R\bar{3}$ (148)	-4.29	0.51
KBiO ₂	16	7.84	7.89	6.55	89.9	131.5	90.0	Monoclinic	$C2/c$ (15)	-4.60	0.33
KBiO ₃	30	5.80	5.80	17.55	90.0	89.9	119.9	Trigonal	$R\bar{3}$ (148)	-4.43	0.36
NaBiS ₂	16	7.90	8.08	7.90	60.8	60.0	60.8	Trigonal	$R\bar{3}m$ (166)	-4.54	0.47
NaBiS ₃	30	6.39	7.66	18.45	81.1	86.0	121.3	Triclinic	$P\bar{1}$ (2)	-3.50	0.47
KBiS ₂	16	7.93	8.65	7.93	62.7	60.0	62.7	Trigonal	$R\bar{3}m$ (166)	-4.78	0.45
KBiS ₃	30	6.34	8.08	17.43	91.8	73.5	114.5	Triclinic	$P\bar{1}$ (2)	-3.61	0.42

Such deviation translates into a deviation of the nonright angle, which is calculated at 131.5° against the experimental assignment at 124.9° . We have repeated the calculation with VASP and obtained similar results for the GGA, which is then the most probable origin of the disagreement with ex-

periments. The presence of the Bi lone pair results in a seesaw molecular geometry, where the Bi local coordination has the C_{2v} point group. The same local geometry is found also for K. The so-formed Bi and K trigonal bipyramids are found to share edges. Finally, for KBiO₃ geometry relaxation from the

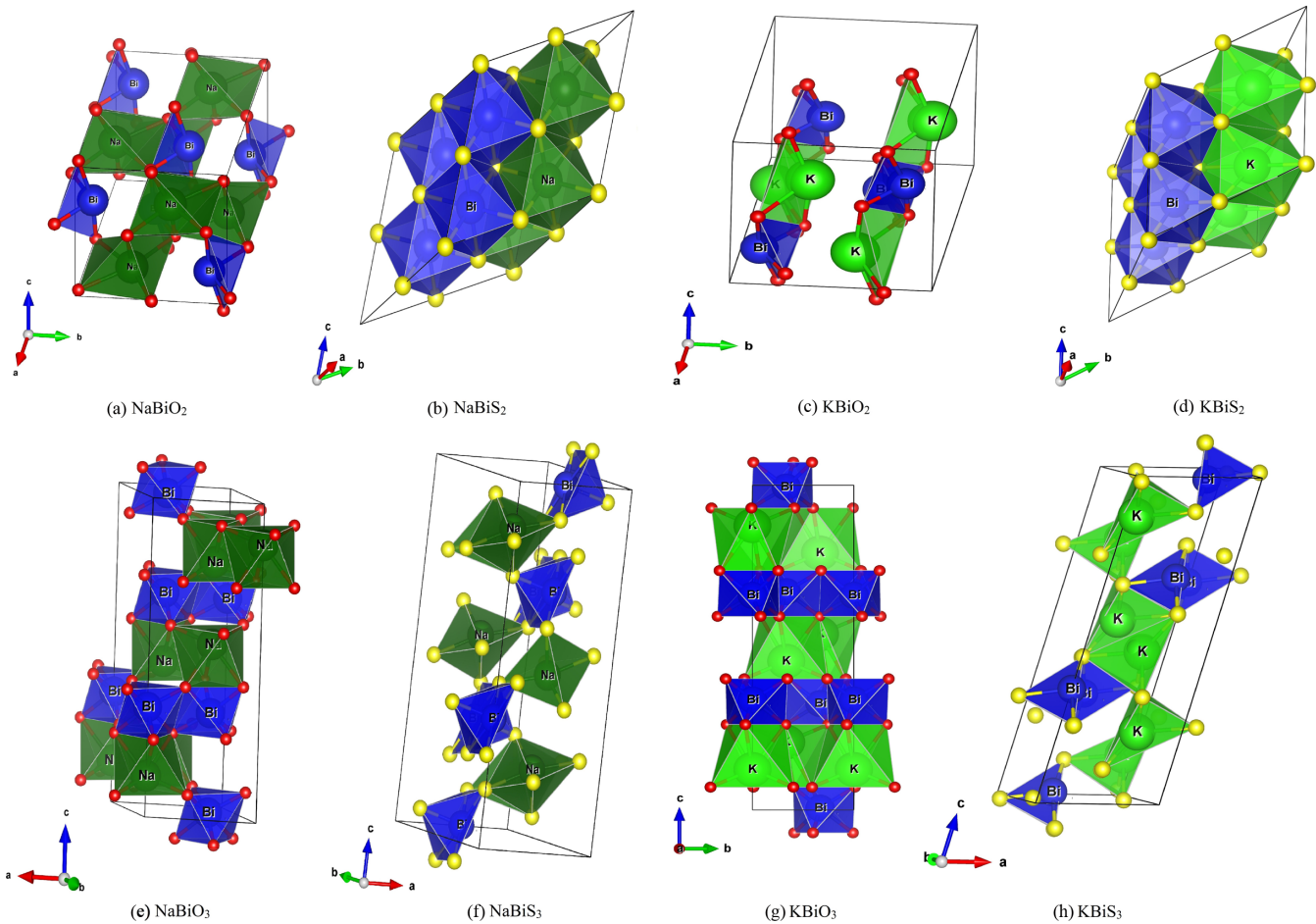


FIG. 1. The crystal structure of (a) NaBiO₂, (b) NaBiS₂, (c) KBiO₂, (d) KBiS₂, (e) NaBiO₃, (f) NaBiS₃, (g) KBiO₃, and (h) KBiS₃. The experimental unit cells of (a) NaBiO₂, (c) KBiO₂, (e) NaBiO₃, and (g) KBiO₃ have been taken from the Materials Project database [58] (see details concerning KBiO₃ in the main text). The initial structures of (b) NaBiS₂, (d) KBiS₂, (f) NaBiS₃, and (h) KBiS₃ have been obtained by replacing O with S in the corresponding oxides (see main text for more details on how the prototypes of NaBiS₂ and KBiS₂ have been constructed). Color code: Bi=blue, O=red, S=yellow, Na=green, K=light green. The colored polygons indicate the local coordination of Bi (green) and the alkali metal cation (blue).

parental NaBiO_3 structure leaves the crystal in the original trigonal $R\bar{3}$ space group, and the only notable difference between NaBiO_3 and KBiO_3 is that the latter presents a significantly larger c/a ratio (3.03 for KBiO_3 against 2.71 for NaBiO_3). Again, the overall structure can be viewed as made of planes of BiO_6 octahedra separated by intercalated K. This presents analogies with the β - Sb_2O_4 structure found for the mixed-valence Bi_2O_4 compound [65].

Given the large electronegativity of O with respect to that of Bi, it is expected that Bi-containing oxides may present large band gaps. A possible strategy to reduce such a band gap is that of replacing O with the less electronegative S, a solution that may also result in more structurally stable compounds [66,67]. In general, there is evidence of band-gap reduction achieved by O to S substitution in perovskites [68,69], and this is attributed to two effects. The presence of the empty S 3d orbitals contributes to lower down the energy of the conduction band, an effect not present for O. On the other hand, the larger ionic radius of S^{2-} (0.184 nm) compared to O^{2-} (0.140 nm) results in a larger cell volume and consequently in less dispersive bands.

As mentioned before, for NaBiS_2 we have constructed the prototype either by replacing O with S in the previously relaxed NaBiO_2 structure or by randomly replacing the Na sites of a NaCl rocksalt supercell with a random distribution of Na and Bi (the Cl sites are all replaced by S) [60]. In this second case, we have employed $2 \times 2 \times 2$ supercells of the rocksalt primitive cell and explored different Na/Bi distributions. Geometrical relaxation starting from the first prototype yields a body-centered tetragonal crystal structure ($I4_1/AMD$), while that originating from the second converges to a trigonal crystal system, with the structure displayed in Fig. 1(b). This latter is lower in energy and therefore it is selected as our final ground-state structure. In such structure, the Na- and Bi-centered octahedra are connected by sharing edges.

Note that the fine details of the structures obtained by relaxing the Na-type $2 \times 2 \times 2$ supercell depend on the specific arrangement of the Na and Bi ions. Namely, although the structural relaxation begins from identical supercells with lattice parameter $a = 7.98$ Å and angle $\alpha = 60^\circ$, the final geometry depends on the specific arrangement of Na and Bi. In particular, the energy minimum is threefold degenerate depending on the elongated lattice vector. If one assumes that the actual structure is the result of an average of such degenerate ground states (note that other nondegenerate configurations are also rather close in energy) and that the average lattice vector is simply the algebraic average of the computed lattice vectors for the $R\bar{3}m$ structure, then we obtain an equivalent rocksalt lattice parameter of 5.63 Å. This is consistent with an old experimental determination of 5.77 Å [59]. We then conclude that actual NaBiS_2 samples are possibly disordered and that the disorder- and thermal-averaged structure is actually cubic, although locally the $R\bar{3}m$ space group is adopted. This is a situation similar to that encountered in halide perovskites, where the high symmetry structure is the result of a macroscopic average of lower-symmetry ones [70].

In contrast, there is no experimental determination for NaBiS_3 , which is predicted triclinic with space group $P\bar{1}$ [see Fig. 1(f)]. In NaBiS_3 , the Bi cations are bonded to five S

anions in a square pyramidal molecular geometry and the Na ones are bonded to five S anions in an irregular tetrahedral molecular geometry.

Moving to Bi compounds containing both S and K, we have treated KBiS_2 in a similar way as NaBiS_2 . Also, in this case relaxation starting from the parental KBiO_2 structure converges to a monoclinic crystal with $C2/c$ space group, namely, it remains with the same structure of KBiO_2 . However, relaxation starting from the substituted rocksalt $2 \times 2 \times 2$ supercell returns us a lower energy trigonal geometry with space group $R\bar{3}m$ and an internal arrangement of K and Bi identical to that of Na and Bi for NaBiS_2 [see Fig. 1(d)]. Again K and Bi are sixfold bonded to S in an octahedral molecular geometry and the octahedra are edge sharing. The same considerations made for NaBiS_2 remain valid here and the average cubic structure is found at a lattice constant of 5.78 Å, to be compared with the experimental estimate of 6.04 Å [59].

The dynamical stability of the cubic and trigonal phases of NaBiS_2 and KBiS_2 have been further investigated by calculating their phonon spectra (see Figs. S1 and S2 of the SM [71]). For KBiS_2 , we have found the cubic phase to be unstable, with imaginary phonon modes across the entire Brillouin zone, while the trigonal phase displays only a tiny region of imaginary frequencies near to the Γ point, which is attributed to a small numerical error. In contrast, both the cubic and trigonal phases of NaBiS_2 appear stable (both phonon spectra show a small instability at Γ due to numerical errors). As such, we conclude that the experimentally measured cubic phases of NaBiS_2 and KBiS_2 are the result of a macroscopic average. In the case of KBiS_2 , this includes differently oriented trigonal phases, while in that of NaBiS_2 it is possible that some local cubic arrangement is also found.

Finally, the crystal structure of KBiS_3 is found to be triclinic with $P\bar{1}$ space group [Fig. 1(h)], namely it has a lower symmetry than its parental trigonal, KBiO_3 . This is the material presenting the lowest degree of bonding. The K and Bi cations are coordinated to four S anions in a seesaw molecular geometry.

B. Thermodynamic stability

Several quantities may provide information about the thermodynamic stability of the compounds investigated. The atomization energy (per atom) is defined as

$$\Delta E_a = E_{\text{total}}/N - \sum_i x_i E_i , \quad (2)$$

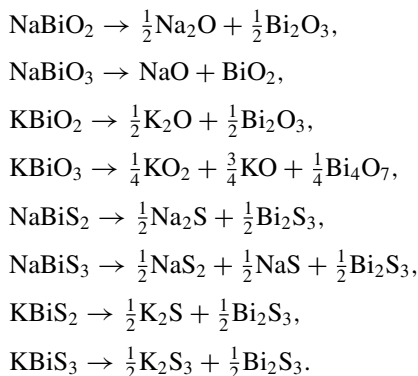
where E_{total} is the total energy per formula unit of the ternary compound, E_i is the atomic energy of the element i , x_i is the atomic fraction, and N is the total number of atom per formula unit. This gives us information about the total bond energy of a solid but says little about its stability. A better quantity is provided by the decomposition energy ΔE_d . It is defined as the total energy difference, per atom in the formula unit, of a given ternary against the binary products of a balanced decomposition reaction, minimized over all possible binaries choices. The decomposition energy thus writes

$$\Delta E_d = \text{Min} \left[\sum_i c_i E_i^{\text{binary}} / N_i \right] - E^{\text{ternary}} / N , \quad (3)$$

where E^{ternary} is the energy per formula unit of the ternary, E_i^{binary} is the energy per formula unit of the binary, c_i are the fractional coefficients needed to balance the reaction, and N and N_i are the total number of atom per formula unit of the ternary and the i th binary, respectively.

With this definition, a ternary compound is stable when $\Delta E_d > 0$, namely when there is no energetically favorable decomposition reaction. In contrast, when $\Delta E_d < 0$ there exists at least one decomposition path whose energy is lower than that of the ternary material under investigation, namely the ternary is thermodynamically unstable against that particular reaction product. Note that in this case, the ternary can still be stabilized by the reaction kinetics, meaning that it can still be metastable. Note also that our definition of ΔE_d does not consider decomposition channels involving alternative ternaries together with the binaries, but it provides a much more stringent criterion for stability than the atomization energy alone [72]. It is, however, unlikely that for any given ternary compound a ternary decomposition path can present a lower total energy than those involving competing binaries, since the enthalpy gain in general decreases with the number of elements contained in a compound [73]. In computing ΔE_d , we have taken the binary prototypes from the Materials Project library [58]. These have been fully relaxed and their electronic structure computed. Note that in the case of polymorphism we have always considered the binary with the lowest energy. Finally, ΔE_d has been calculated using the Pymatgen library [74–76].

Our results are reported in Table I, while the list of the most stable decomposition of each of the eight compounds is presented below.



In general, we find that for all compounds ΔE_d is positive, meaning that they are all stable, as expected from experimental evidence. In the case of oxides, the $A\text{BiX}_3$ stoichiometry is more robust against decomposition than the $A\text{BiX}_2$ one, suggesting that in this class of materials Bi has a preference for the +5 oxidation state, despite that most of the Bi chemistry [77] is based on the +3. Such difference is significantly more pronounced for Na-containing compounds than K-containing ones. The same is not valid for sulphides, for which the two stoichiometries have essentially identical stability.

C. Elastic and mechanical properties

The elastic stiffness constants C_{ij} are calculated for all the compounds in order to determine the bulk modulus B ,

the shear modulus G , the Young's modulus Y , and the Poisson's ratio ν . Unfortunately, to the best of our knowledge, experimental and theoretical elastic constants for the eight alkali-metal based bismuth chalcogenides are not available, so that our calculations cannot be compared with literature and constitute the first assessment made of the elastic properties of this class of materials. We have then used the C_{ij} 's to evaluate the mechanical stability of our compounds according to the Born elastic stability criteria [78,79].

Let us start our discussion from the mechanical stability analysis. The eight compounds investigated fall into three crystal structure systems, namely the trigonal, the monoclinic, and the triclinic, with the Born elastic stability conditions varying for the different crystal lattices. The monoclinic and triclinic structures have 13 and 21 independent elastic constants, respectively. The stability conditions for these two crystal systems could be evaluated by demonstrating that the leading principal minors of the elastic stiffness constants matrix are positive [80]. Such condition for the trigonal structure at zero pressure, for instance, reads

$$\begin{aligned} C_{11} &> |C_{12}|, C_{11}, C_{33}, C_{44} > 0, \\ [(C_{11} + C_{12})C_{33} - 2C_{13}^2] &> 0, \\ [(C_{11} - C_{12})C_{44} - 2C_{14}^2] &> 0. \end{aligned} \quad (4)$$

The elastic stiffness constants of all the compounds are reported in Table S1 [71] of the Supplemental Material (SM). When these are input in the Born elastic stability criteria, we found that all compounds are mechanically stable at zero pressure.

Then B , G , Y , and ν can be computed directly from the elastic tensor. The explicit expressions for the trigonal system [81] are provided here in Eq. (5) through Eq. (10), while the corresponding ones for the monoclinic and triclinic systems can be easily found in literature [82,83]. In the definitions provided, the subscripts 'V', 'R,' and 'H' indicate the Voigt, Reuss, and Hill approximations. The Voigt and Reuss equations relate B and G to the elastic constants C_{ij} and their compliances $S_{ij} = C_{ij}^{-1}$, while the Hill approximation is the arithmetic mean of the Voigt and Reuss bounds [84,85]. It must be noted that the Voigt approximation provides an upper bound to the actual elastic moduli, while the Reuss one returns the lower limit.

$$B_V = \frac{1}{9}(2C_{11} + C_{33}) + \frac{2}{9}(C_{12} + 2C_{13}), \quad (5)$$

$$G_V = \frac{1}{15}(2C_{11} + C_{33} - C_{12} - 2C_{13}) + \frac{1}{5}\left(2C_{44} + \frac{C_{11} - C_{12}}{2}\right), \quad (6)$$

$$B_R = \frac{1}{(2S_{11} + S_{33}) + 2(S_{12} + 2S_{13})}, \quad (7)$$

$$G_R = \frac{15}{4(2S_{11} + S_{33} - S_{12} - 2S_{13}) + 6(S_{44} + S_{11} - S_{12})}, \quad (8)$$

$$Y = \frac{9B_H G_H}{3B_H + G_H}, \quad \nu = \frac{(3B_H - 2G_H)}{2(3B_H + G_H)}, \quad (9)$$

$$B_H = \frac{1}{2}(B_V + B_R), \quad G_H = \frac{1}{2}(G_V + G_R). \quad (10)$$

TABLE II. The bulk modulus B , shear modulus G , Young's modulus Y , Poisson's ratio ν , and Pugh's ratio (B_H/G_H) calculated for all the alkali-metal based bismuth ternary chalcogenides. The subscripts V, R, and H indicate the Voigt, Reuss, and Hill approximations, respectively.

Compound	Bulk modulus (GPa)			Shear modulus (GPa)			Young's modulus (GPa)	Poisson's ratio	Pugh's ratio
	B_V	B_R	B_H	G_V	G_R	G_H			
NaBiO ₂	45.57	27.47	36.52	24.42	1.07	12.74	34.25	0.34	2.87
KBiO ₂	41.46	32.13	36.80	21.51	1.17	11.34	30.85	0.36	3.25
NaBiO ₃	76.03	57.77	66.90	41.71	38.52	40.12	100.30	0.25	1.67
KBiO ₃	66.75	46.00	56.38	30.85	26.06	28.46	73.08	0.28	1.98
NaBiS ₂	55.68	54.23	54.96	38.28	32.73	35.50	87.64	0.23	1.56
KBiS ₂	57.54	57.27	57.40	40.89	29.84	35.36	88.02	0.24	1.62
NaBiS ₃	28.36	18.40	23.38	11.12	7.27	9.20	24.39	0.33	2.54
KBiS ₃	28.08	20.97	24.52	12.94	9.47	11.20	29.17	0.30	2.19

Table II summarizes all the results. The bulk and shear moduli describe the hardness of a material, while the Young's modulus measures its stiffness [86]. The bulk, shear, and Young's moduli of the compounds investigated are found to decrease as the crystal symmetry is reduced, namely all compounds in the trigonal phase possess bulk, shear, and Young's moduli larger than those of the monoclinic and triclinic phases, with NaBiO₃ and KBiO₃ displaying the highest values of B_H , G_H , and Y . Interestingly, we find oxides to be stiffer than sulphides for the $ABiX_3$ stoichiometry, while the situation is reversed for the $ABiX_2$ one. Interestingly, NaBiO₂ and KBiO₂ exhibit the largest difference in the Voigt and Reuss bounds, while NaBiS₂ and KBiS₂ the smallest.

The Poisson's ratio serves as a valuable indicator of the plasticity of a material. When the value exceeds 0.26, the material is predicted to be ductile, otherwise it is brittle [87]. Hence, it is found that all compounds in the trigonal phase, except KBiO₃, are brittle, while all compounds with monoclinic and triclinic phase are ductile. The Pugh's B/G ratio is another reference to predict the brittleness or ductility of a material [88]. If a material possesses a B/G value larger than 1.75, it is predicted ductile. On this ground, the brittleness of the compounds under investigation is found to reduce as one moves from the trigonal to the monoclinic and finally to the triclinic phase. KBiO₂ is expected to have the highest ductility, while NaBiS₂ to be the most brittle.

D. Electronic structure properties

Let us now discuss the features of the GGA band structures of the eight compounds investigated by starting from the oxides. In this section we will also report results obtained with the GLLB-SC functional, which improves the description of the band over the GGA. Since Na- and K-containing oxides have identical lattice structures with relatively similar lattice parameters, their electronic structure is very similar. Hence, we present, in Figs. 2 and 3, the band structure, respectively, of NaBiO₂ and NaBiO₃, while those of the corresponding KBiO₂ and KBiO₃ are displayed in the SM (Figs. S3 and S4, respectively [71]).

NaBiO₂ and KBiO₂ are two direct-band-gap semiconductors with the band gap located at the center of the Brillouin zone, Γ . Both the conduction and valence bands are rather dispersive around their edges, with the valence band presenting a region of low dispersion between 1.5 eV and 2 eV (1 eV and

1.5 eV) for NaBiO₂ (KBiO₂) below the valence band maximum (VBM). The projected density of state (PDOS) returns us a valence band mostly associated with O- p states, but with contributions also from Bi- s and Bi- p orbitals, fully consistent with the O²⁻ and Bi³⁺ oxidation states and with a significant O- p /Bi- p orbital hybridization. In particular, the Bi-derived fraction of the PDOS is more pronounced at the VBM and it is responsible for the relatively large band dispersion, while the flat valence manifold is associated to the dominant O- p character. In contrast, the conduction band is mostly associated to Bi- p , again with an hybridization contribution from the O- p orbital. The inclusion of spin-orbit coupling (SOC) in the calculation has little effect on the band structure, except for a marginal reduction of the conduction band bandwidth. This moves slightly the conduction band maximum (CBM) to higher energies, thus increasing the band gap. The GGA band gap of NaBiO₂ (KBiO₂) is around 1.35 eV (1.80 eV), whereas its GLLB-SC counterpart is around 1.93 eV (2.47 eV) (all the calculated band gaps are reported in Table III).

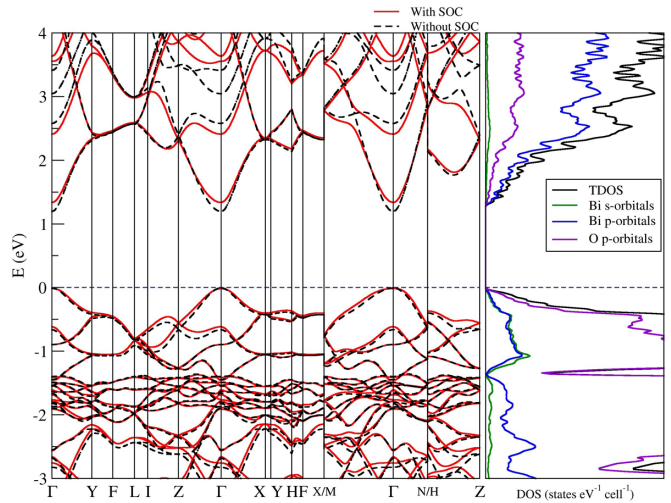


FIG. 2. The calculated DFT-GGA energy band structure and PDOS of NaBiO₂. The VBM and CBM lie both at the Γ point, making it a direct-gap semiconductor. The red and the dashed-black lines represent, respectively, the bands calculated with and without including spin-orbit coupling (SOC). The PDOS on the right-hand side is for the band structure calculated with SOC.

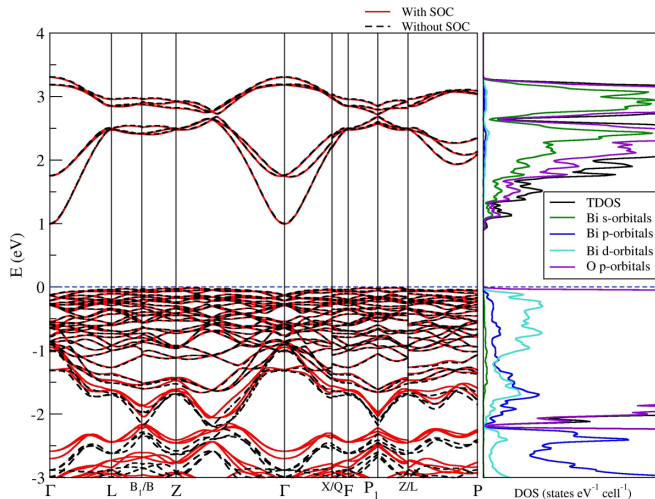


FIG. 3. The calculated DFT-GGA energy band structure and PDOS of NaBiO_3 . The compound is an indirect band-gap semiconductor with its VBM lying between P_1 and Z and the CBM at Γ . The red and the dashed-black lines represent, respectively, the bands calculated with and without including spin-orbit coupling (SOC). The PDOS on the right-hand side is for the band structure calculated with SOC.

In contrast, both NaBiO_3 (Fig. 3) and KBiO_3 (Fig. S4 of the SM [71]) are calculated as indirect band-gap semiconductors with the CBM placed at Γ and the VBM at a low-symmetry k point located between P_1 and Z. The main feature of the band structure, however, is that the top of the valence band has very little dispersion, so that the direct and indirect band gaps are essentially identical. The rather flat VBM is completely determined by the O- p orbitals, while the hybridization contribution from the Bi s and p shells is significantly reduced with respect to the case of the ABiO_2 stoichiometry and it is evident only in the lower part of the valence manifold. This reflects the fact that now Bi is close to the nominal oxidation state of +5 (the s shell is empty). A second important feature is that also

the conduction band has an O- p character, indicating that not all the O ions are saturated. The Bi- p empty conduction band (not displayed here) is well separated from the O- p one and is placed at energies between 6 eV and 8 eV above the Fermi level (for both NaBiO_3 and KBiO_3).

As a consequence, the band gaps of the ABiO_3 compounds are between O- p states and are lower than their ABiO_2 counterparts. We obtain the PBE (GLLB-SC) gaps of 1.02 eV (1.80 eV) and 1.17 eV (1.82 eV), respectively, for NaBiO_3 and KBiO_3 . The experimental determination of the band gaps available in the literature for NaBiO_3 and KBiO_3 are based on UV-vis diffused-reflectance spectra [39,89]. This returns us a value of 2.6 eV and 2.1 eV, respectively, for NaBiO_3 and KBiO_3 , which are consistent with our data considering the systematic GGA underestimation of the band gaps. The GLLB-SC description of the band gap seems to improve the results, although our theoretical estimate remains smaller than the experimental observation.

Note that the role of the alkali metals is minor but not negligible. In general, we find a systematic band gap increase as the ionic radius of the alkali metal gets larger. This appears to be related to the general increase in cell volume and hence to the weakening of the orbital hybridization. Enforcing this argument is the bandwidth reduction when going from Na- to K-based compounds, which is, for instance, particularly evident in the conduction bands of NaBiO_2 and KBiO_2 . Finally, we observe that SOC has little effect on ABiO_3 compounds. Both the CBM and VBM are almost unaffected by SOC, as expected from their O- p character, and the only notable changes in the band structure (in the energy range considered in Fig. 3) are in the valence manifold for energies lower than 2 eV from the VBM. This is the only energy region where the PDOS shows a non-negligible Bi- p contribution. Let us now turn our attention to the band structures of the sulphides, again, starting from the ABiS_2 composition. Broadly speaking, NaBiS_2 (Fig. 4) and KBiS_2 (Fig. S5 of the SM [71]) have an electronic structure similar to that of their oxide counterparts, namely they present a valence band with a strong S- p

TABLE III. Energy gaps calculated using the Kohn-Sham spectrum obtained with PBE (ΔE_{PBE}), GLLB-SC (ΔE_{GLLBSc}), and extracted from the imaginary part of the RPA-PBE dielectric function (optical gap) ΔE_{opt} are reported. For comparison, we report both the direct and indirect gaps calculated using the PBE functional. E_R is the experimentally reported band gap. Two compounds, namely NaBiO_2 and KBiO_2 , are direct band gap materials, while all the others are indirect. Note that the band gaps reported from literature for KBiO_3 , NaBiS_2 , and KBiS_2 are always associated to the cubic structure, while our results are for their trigonal phase (see discussion). Also, the reported energy gaps, E_R , for NaBiO_2 and KBiO_2 are theoretical values (no experimental determination exists). In the last two columns, we report the average static dielectric function $\bar{\epsilon}$ and its variance $\Delta \epsilon$ (see definition in the main text).

Compound	Energy gaps (eV)						
	E_{PBE}		$E_{\text{GLLB-SC}}$	E_{opt}	E_R	$\bar{\epsilon}$	$\Delta \epsilon$
Direct	Indirect						
NaBiO_2	1.35		1.93	1.42	1.60 [33]	2.35	0.68
NaBiO_3	1.16	1.02	1.80	1.33	2.60 [89]	2.58	0.09
KBiO_2	1.80		2.47	1.89	2.00 [34]	2.16	0.66
KBiO_3	1.25	1.17	1.82	1.47	2.10 [39]	2.36	0.23
NaBiS_2	2.10	1.51	2.03	2.19	0.44–1.41 [41,60,92,93]	5.79	0.02
NaBiS_3	0.89	0.80	1.24	0.90		3.82	1.90
KBiS_2	2.19	1.64	2.15	2.14	0.90, 1.61 [41,93]	5.31	0.06
KBiS_3	1.44	1.26	1.79	1.49		4.58	1.84

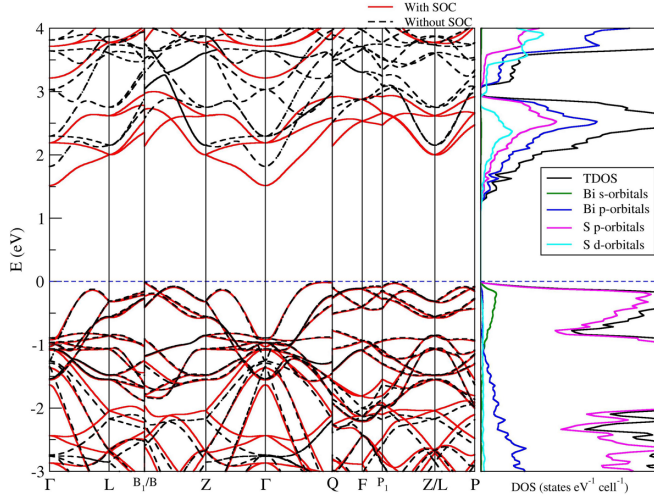


FIG. 4. The calculated DFT energy band structure and PDOS of NaBiS₂. The compound is an indirect band-gap semiconductor with its VBM at Q and the CBM at Γ . The red and the dashed-black lines represent, respectively, the bands calculated with and without including spin-orbit coupling (SOC). The PDOS on the right-hand side is for the band structure calculated with SOC.

character and hybridization with the Bi-*s* and Bi-*p* shells at its top. The dispersion is significantly less pronounced than in the oxide case owing a further unit cell volume increase. Both NaBiS₂ and KBiS₂ are indirect band-gap semiconductors with the CBM at Γ . The position of the VBM is at Q for NaBiS₂ and at a low-symmetry point along the Z-to- Γ direction for KBiS₂. Notably for KBiS₂, the VBM is almost degenerate with several other minima extremely close in energy and all located at low symmetry points in the Brillouin zone (e.g., Γ to Q, Γ to L).

The inclusion of SOC has a much more pronounced effect than in the case of the oxides. In fact, there is a split of the conduction band into a lower and an upper manifold with a net reduction of the band gap with respect to that calculated without considering spin orbit. Such drastic reduction is similar to what was found for Pb-based halide perovskites [90,91], which share with the compounds investigated here the octahedral local coordination of the heavy metal (Pb and Bi). In contrast, the local coordination of Bi in ABiO₂ is quasitetrahedral, and this seems to be the main difference in the behavior of the sulphides and oxides against SOC. In any case, for both NaBiS₂ and KBiS₂, the band gap remains larger than that of their corresponding oxides. There are a number of experimental determinations of the band gap of NaBiS₂ and KBiS₂ (see Table III). These seem to return the measured band gaps rather narrow and constantly smaller than those computed with the GGA and the GLLB-SC functional. Such a result is somehow unexpected, given the consistent GGA underestimation of the band gaps and the typical good description given by GLLB-SC. However, it has to be noticed that in all the experimental works [60,92,93] the lattice structure is reported cubic, although no further crystallographic characterization is provided. Our calculated band gap are for the trigonal structure. As speculated before, we believe that the experimental structure is actually a macro-

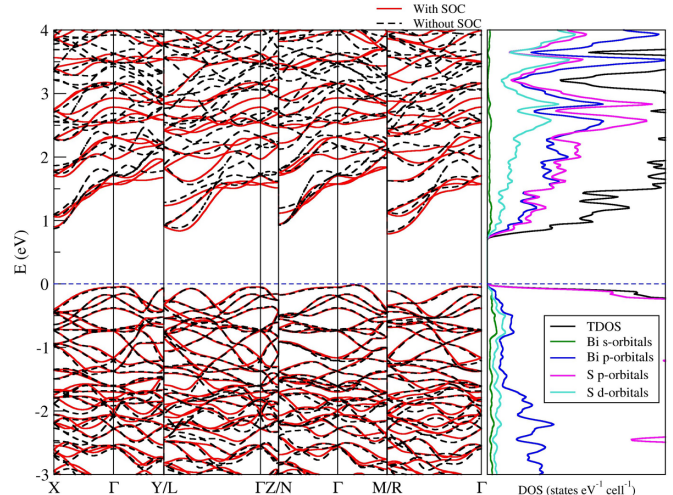


FIG. 5. The calculated DFT energy band structure and PDOS of NaBiS₃. The compound is an indirect band-gap semiconductor with its VBM lying between Γ and M and the CBM at R. The red and the dashed-black lines represent, respectively, the bands calculated with and without including spin-orbit coupling (SOC). The PDOS on the right-hand side is for the band structure calculated with SOC.

scopic average of local trigonal lattices. Hence, the measured band gap is the result of such average, which needs to be taken over the crystal structure orientation and the site occupation. We then expect that the actual band gap will be significantly smaller than that computed for a homogeneous trigonal lattice with an ordered site-occupation configuration. As a further test we have computed the band gaps of the metastable cubic structures of NaBiS₂ and KBiS₂. PBE returns values of 1.46 eV and 1.56 eV for NaBiS₂ (lattice constant 5.76 Å) and KBiS₂ (lattice constant 5.95 Å), respectively. These are rather similar to those obtained for the trigonal phases and again systematically larger than what measured. Such discrepancy between predictions and experiments appears to corroborate further the idea that actual samples are not in a single cubic phase, but they are rather a macroscopic average of equivalent trigonal ones.

Finally, we look at NaBiS₃ (Fig. 5) and KBiS₃ (Fig. S6 of the SM [71]). Their PDOSs have some similarities with those computed for the oxides with the same stoichiometry, in particular, for what concerns the top of the valence band, which is completely dominated by O-*p* states. The conduction band instead appears to present a strong mixture between O-*p* and Bi-*p* contributions, consistent with the nominal Bi⁺⁵ valence configuration. This is different from what was found for ABiO₃, in which the O and Bi contributions to the conduction band are well separated. Such difference is a consequence of both the lower electron affinity of S with respect to O and of the different local Bi coordination in oxides and sulphides. Also, notable is the presence of a Bi-*d* orbital contribution across the entire valence manifold.

Both NaBiS₃ and KBiS₃ are predicted to be indirect gap semiconductors. NaBiS₃ has the VBM at a low-symmetry point along the Γ -to-M direction and the CBM at R, while for KBiS₃ the VBM is M and the CBM is at X. In both cases, there are other points in the Brillouin zone with energy close

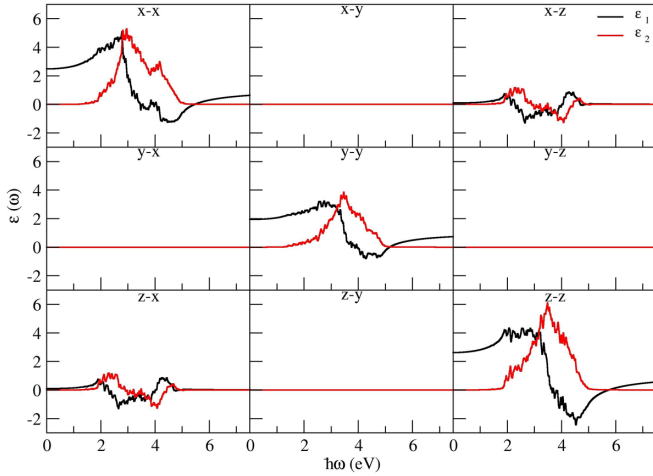


FIG. 6. Real, $\varepsilon_1(\omega)$ (black line), and imaginary, $\varepsilon_2(\omega)$ (red line), component of the dielectric tensor of NaBiO_2 as a function of energy.

to that of the band extremal points owing to the relatively low dispersion. The PBE (GLLB-SC) gap values are 0.89 eV (1.24 eV) and 1.26 eV (1.79 eV), respectively, for NaBiS_3 and KBiS_3 . As expected, they are smaller than those of the corresponding oxides and, as in the oxides case, the largest gap is associated to the alkaline metal presenting the largest ionic radius K. We are not aware of any experimental or theoretical determination of the gap, so that our results remain the only available. Finally, we observe that SOC has almost no effect on the top of the valence band, which is primarily dominated by S-p states, while it distorts the lower part of the conduction one, where the Bi content to the PDOS is larger. Notably, such distortion is not associated to a significant alteration of the size of the band gap.

E. Dielectric properties

The interband contribution to the linear dielectric tensor calculated within the RPA over the PBE band structure for all the eight compounds are now discussed. The calculations were carried out for an energy range between 0 eV and 7.5 eV in order to include the infrared, visible, and ultraviolet region of the electromagnetic spectra. In particular, for all compounds we compute both the real $\varepsilon_1(\omega)$ and imaginary $\varepsilon_2(\omega)$ part of the dielectric function and we define the optical gap at the minimum onset of the three diagonal components of $\varepsilon_2(\omega)$. Let us start our analysis from NaBiO_2 and KBiO_2 , whose dielectric functions are displayed in Fig. 6 and Fig. S7 of the SM [71], respectively. As expected from the rather similar electronic structure, NaBiO_2 and KBiO_2 have very similar dielectric functions. The diagonal component of the dielectric tensors are relatively anisotropic, as expected from the low symmetry lattice, and the only non-negligible off-diagonal component is the xz one (identical to the zx one since ε is a symmetric tensor). The optical band gap is found for both NaBiO_2 and KBiO_2 in the yy component and it coincides with the direct Kohn-Sham band gap at Γ (see Table III). This means that the direct transition from the VBM to the CBM is allowed. Note that the optical gap does not exactly

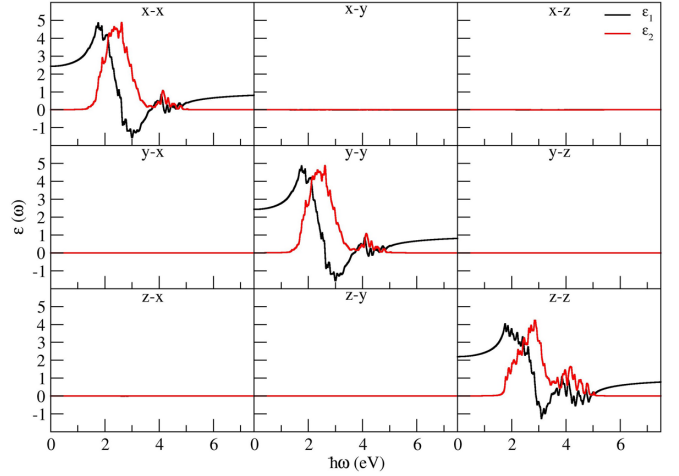


FIG. 7. Real, $\varepsilon_1(\omega)$ (black line), and imaginary, $\varepsilon_2(\omega)$ (red line), component of the dielectric tensor of NaBiO_3 as a function of energy.

coincide with the Kohn-Sham one, because of the broadening introduced when computing the dielectric function.

The dielectric functions of the ABiO_3 compounds are presented in Fig. 7 (NaBiO_3) and Fig. S8 of the SM (KBiO_3 [71]). In this case, the dielectric tensor is rather isotropic and diagonal, owing to the high symmetry of the crystal structure. For both NaBiO_3 and KBiO_3 , we find that the optical gap is about 0.2 eV larger than the direct Kohn-Sham one (PBE), indicating that transitions at the band edges are forbidden, or at least highly suppressed (the lowest among the conduction bands has high dispersion, so that the density of transitions is low). In fact, the onset of $\varepsilon_2(\omega)$ corresponds to excitations from the VBM to the second of the conduction bands.

Moving to the sulphides, the dielectric constant profiles are shown in Figs. S7 through S12 of the SM [71]. In all cases, the tensor is nondiagonal and generally anisotropic. Such anisotropy appears genuine for the ABiS_3 compounds, while for the ABiS_2 we have to notice, once again, that the results reported here correspond to a specific arrangement of the Bi and Na/K ions. Thus, it is reasonable to expect that such anisotropy will be strongly suppressed, once the appropriate macroscopic average over the atomic distribution and distortion is taken. The optical band gaps of NaBiS_2 and KBiS_2 are generally larger than the Kohn-Sham ones by about 0.5 eV and correspond to the first available direct transitions, namely the optical gap is simply the Kohn-Sham direct gap. As noted before, these band gaps are larger than those reported in the literature (see discussion in the previous section). Finally, for NaBiS_3 and KBiS_3 , the optical band gap are only marginally larger than the Kohn-Sham one and again correspond to the first available direct transition.

To conclude this section we discuss the static dielectric constant. The average value of its diagonal components, $\bar{\varepsilon}$, and the corresponding variance, $\Delta\varepsilon = |\max_\alpha \varepsilon_{\alpha\alpha} - \min_\alpha \varepsilon_{\alpha\alpha}|$, are reported in the last two columns of Table III, while detailed information about the full static dielectric tensor is included in the SM [71]. In general, we find the sulphides to have an average dielectric constant larger than that of the oxides, with Na-based sulphide presenting the largest values. Furthermore, as expected, we find that the asymmetry of the dielectric

constant, as measured via $\Delta\epsilon$, follows the symmetry of the associated lattice structure. The triclinic $ABiS_3$ and monoclinic $ABiO_3$ compounds present the largest variations, while for the remaining trigonal structures the diagonal elements of the static dielectric tensor are rather similar to each other. This trend follows closely to that found for the dynamic dielectric functions.

IV. CONCLUSIONS

Motivated by the need for finding a Pb-free replacement of $MAPbI_3$ as light-harvesting media, we have presented an extensive computational study of the structural, thermodynamic, elastic, electronic, and dielectric properties of alkali-metal-based bismuth ternary chalcogenides. The structures of the various compounds have been calculated in agreement with available crystallographic data, with the exception of $NaBiS_2$ and $KBiS_2$, for which DFT has returned us a trigonal instead of a cubic structure. Consistency between theory and experiments is then reached by assuming that the experimental samples, known to have the site-occupation disorder, are a macroscopic average of the various equivalent trigonal structures.

We have found that all the compounds investigated are thermodynamically and mechanically stable. An analysis of their elastic properties has revealed that the bulk, shear, and Young's moduli get smaller as the crystal structure goes from trigonal to monoclinic and finally to triclinic. These compounds present a semiconducting band structure with DFT GGA gaps ranging between 0.80 eV and 1.80 eV. The optical gaps are marginally larger than the quasiparticle ones owing to the fact that they are indirect. Notably, in all cases the difference between the direct and indirect gap is not large, since the extremal bands are relatively flat. $NaBiO_2$ and $KBiO_2$

have a direct gap. Considering the well-known tendency of the GGA to underestimate the quasiparticle gap, we expect these compounds to absorb light in the early blue region of the electromagnetic spectrum. On the grounds of their thermodynamic stability, electronic, and optical properties, we foresee these materials as alternative lead-free visible-light absorbing semiconducting materials. In all compounds, the conduction band is dominated by Bi-p orbitals as suggested by the Bi^{3+} and Bi^{5+} nominal oxidation state. This is similar to what was found for lead-based halides hybrid perovskites, and we expect for the Bi-based compounds the exciton binding energy to be small. $NaBiO_3$ and $KBiO_3$ are the exceptions, since the band gap is between O-p orbitals. A small exciton binding energy together with an indirect gap make these compounds interesting [94] as potential media for photocatalysis and water splitting. This is an area that certainly deserves further study, which is currently ongoing.

ACKNOWLEDGMENTS

S.K.R. thanks Colibaba Anais Stefana, Rui Dong, Carlo Motta, and Florian Knoop for the useful discussions. This work is supported by Institute of Technology Sligo President's Bursary Award under the Grant No. PPRES050. S.S. thanks the Irish Research Council (IRCLA/2019/127) for financial support. F.E. thanks the Qatar National Research Fund (QNRF) through the National Priorities Research Program (NPRP8-090-2-047). Computational resources have been provided by the Trinity Centre for High Performance Computing (TCHPC) (Project Code: HPC_16_00953) and Irish Centre for High-End Computing (ICHEC) (Project Codes: isphy001c and isphy002c).

-
- [1] D. Sica, O. Malandrino, S. Supino, M. Testa, and M. C. Lucchetti, *Renew. Sust. Energ. Rev.* **82**, 2934 (2018).
 - [2] M. Tao, *Terawatt Solar Photovoltaics* (Springer, London, 2014), pp. 9–20.
 - [3] D. Ginley, M. A. Green, and R. Collins, *MRS Bull.* **33**, 355 (2008).
 - [4] C. Deibel and V. Dyakonov, *Rep. Prog. Phys.* **73**, 096401 (2010).
 - [5] A. Hagfeldt, G. Boschloo, L. Sun, L. Kloo, and H. Pettersson, *Chem. Rev.* **110**, 6595 (2010).
 - [6] M. Yamaguchi, *Sol. Energy Mater. Sol. Cells* **75**, 261 (2003).
 - [7] T. M. Brenner, D. A. Egger, L. Kronik, G. Hodes, and D. Cahen, *Nat. Rev. Mater.* **1**, 15007 (2016).
 - [8] M. Wolf, *Proc. IREE* **48**, 1246 (1960).
 - [9] A. Poglitsch and D. Weber, *J. Chem. Phys.* **87**, 6373 (1987).
 - [10] D. Mitzi, C. Feild, W. Harrison, and A. Guloy, *Nature (London)* **369**, 467 (1994).
 - [11] H.-S. Kim, C.-R. Lee, J.-H. Im, K.-B. Lee, T. Moehl, A. Marchioro, S.-J. Moon, R. Humphry-Baker, J.-H. Yum, J. E. Moser *et al.*, *Sci. Rep.* **2**, 591 (2012).
 - [12] M. A. Green, E. D. Dunlop, J. Hohl-Ebinger, M. Yoshita, N. Kopidakis, and A. W. Y. Ho-Baillie, *Progress in Photovoltaics: Research and Applications* **28**, 3 (2019).
 - [13] M. M. Lee, J. Teuscher, T. Miyasaka, T. N. Murakami, and H. J. Snaith, *Science* **338**, 643 (2012).
 - [14] H. Zhou, Q. Chen, G. Li, S. Luo, T.-b. Song, H.-S. Duan, Z. Hong, J. You, Y. Liu, and Y. Yang, *Science* **345**, 542 (2014).
 - [15] T. Salim, S. Sun, Y. Abe, A. Krishna, A. C. Grimsdale, and Y. M. Lam, *J. Mater. Chem. A* **3**, 8943 (2015).
 - [16] Y. Zhao and K. Zhu, *J. Phys. Chem. Lett.* **5**, 4175 (2014).
 - [17] T.-B. Song, Q. Chen, H. Zhou, C. Jiang, H.-H. Wang, Y. M. Yang, Y. Liu, J. You, and Y. Yang, *J. Mater. Chem. A* **3**, 9032 (2015).
 - [18] S. De Wolf, J. Holovsky, S.-J. Moon, P. Lolper, B. Niesen, M. Ledinsky, F.-J. Haug, J.-H. Yum, and C. Ballif, *J. Phys. Chem. Lett.* **5**, 1035 (2014).
 - [19] Y.-Y. Zhang, S. Chen, P. Xu, H. Xiang, X.-G. Gong, A. Walsh, and S.-H. Wei, *Chin. Phys. Lett.* **35**, 036104 (2018).
 - [20] D. P. McMeekin, G. Sadoughi, W. Rehman, G. E. Eperon, M. Saliba, M. T. Hörranter, A. Haghhighirad, N. Sakai, L. Korte, B. Rech *et al.*, *Science* **351**, 151 (2016).
 - [21] N. K. Noel, S. D. Stranks, A. Abate, C. Wehrenfennig, S. Guarnera, A.-A. Haghhighirad, A. Sadhanala, G. E. Eperon, S. K. Pathak, M. B. Johnston *et al.*, *Energy Environ. Sci.* **7**, 3061 (2014).

- [22] C. N. Savory, A. Walsh, and D. O. Scanlon, *ACS Energy Lett.* **1**, 949 (2016).
- [23] W.-J. Yin, J.-H. Yang, J. Kang, Y. Yan, and S.-H. Wei, *J. Mater. Chem. A* **3**, 8926 (2015).
- [24] M. Lyu, J.-H. Yun, M. Cai, Y. Jiao, P. V. Bernhardt, M. Zhang, Q. Wang, A. Du, H. Wang, G. Liu *et al.*, *Nano Research* **9**, 692 (2016).
- [25] X. Gonze, J.-P. Michenaud, and J.-P. Vigneron, *Phys. Scr.* **37**, 785 (1988).
- [26] F. Vines, M. Bernechea, G. Konstantatos, and F. Illas, *Phys. Rev. B* **94**, 235203 (2016).
- [27] B. Ghosh, B. Wu, H. K. Mulmudi, C. Guet, K. Weber, T. C. Sum, S. Mhaisalkar, and N. Mathews, *ACS Appl. Mater. Interfaces* **10**, 35000 (2018).
- [28] R. L. Hoye, L. C. Lee, R. C. Kurchin, T. N. Huq, K. H. Zhang, M. Sponseller, L. Nienhaus, R. E. Brandt, J. Jean, J. A. Polizzotti *et al.*, *Adv. Mater.* **29**, 1702176 (2017).
- [29] F. Demartin, C. Gramaccioli, and I. Campostrini, *Mineral. Mag.* **74**, 141 (2010).
- [30] L. C. Lee, T. N. Huq, J. L. MacManus-Driscoll, and R. L. Hoye, *APL Mater.* **6**, 084502 (2018).
- [31] B.-W. Park, B. Philippe, X. Zhang, H. Rensmo, G. Boschloo, and E. M. Johansson, *Adv. Mater.* **27**, 6806 (2015).
- [32] S. Öz, J.-C. Hebig, E. Jung, T. Singh, A. Lepcha, S. Olthof, F. Jan, Y. Gao, R. German, P. H. van Loosdrecht *et al.*, *Sol. Energy Mater. Sol. Cells* **158**, 195 (2016).
- [33] E. Keller and C. Röhr, *Zeit. Krist.-Crystalline Materials* **223**, 431 (2008).
- [34] N. Zoche and M. Jansen, *Z. Anorg. Allg. Chem.* **624**, 205 (1998).
- [35] N. Kumada, N. Kinomura, and A. Sleight, *Mater. Res. Bull.* **35**, 2397 (2000).
- [36] J. Liu, S. Chen, Q. Liu, Y. Zhu, and J. Zhang, *Chem. Phys. Lett.* **572**, 101 (2013).
- [37] S. Chen, Z. Cao, and X. Fu, *Mater. Chem. Phys.* **142**, 748 (2013).
- [38] L. Cheng and Y. Kang, *Mater. Lett.* **117**, 94 (2014).
- [39] R. Ramachandran, M. Sathiya, K. Ramesha, A. Prakash, G. Madras, and A. Shukla, *J. Chem. Sci.* **123**, 517 (2011).
- [40] J. Boon, *Recl. Trav. Chim.* **63**, 32 (1944).
- [41] B. Gabrel'yan, A. Lavrentiev, I. Y. Nikiforov, and V. Sobolev, *J. Struct. Chem.* **49**, 788 (2008).
- [42] V. Blum, R. Gehrke, F. Hanke, P. Havu, V. Havu, X. Ren, K. Reuter, and M. Scheffler, *Comput. Phys. Commun.* **180**, 2175 (2009).
- [43] J. P. Perdew, M. Ernzerhof, and K. Burke, *J. Chem. Phys.* **105**, 9982 (1996).
- [44] J. D. Head and M. C. Zerner, *Chem. Phys. Lett.* **122**, 264 (1985).
- [45] T. Bučko, S. Lebègue, J. Hafner, and J. G. Angyan, *Phys. Rev. B* **87**, 064110 (2013).
- [46] G.-X. Zhang, A. Tkatchenko, J. Paier, H. Appel, and M. Scheffler, *Phys. Rev. Lett.* **107**, 245501 (2011).
- [47] C. Motta, F. El-Mellouhi, S. Kais, N. Tabet, F. Alharbi, and S. Sanvito, *Nat. Commun.* **6**, 7026 (2015).
- [48] A. Tkatchenko and M. Scheffler, *Phys. Rev. Lett.* **102**, 073005 (2009).
- [49] C. Ambrosch-Draxl and J. O. Sofo, *Comput. Phys. Commun.* **175**, 1 (2006).
- [50] G. Kresse and J. Furthmüller, *Phys. Rev. B* **54**, 11169 (1996).
- [51] P. E. Blöchl, *Phys. Rev. B* **50**, 17953 (1994).
- [52] O. Gritsenko, R. van Leeuwen, E. van Lenthe, and E. J. Baerends, *Phys. Rev. A* **51**, 1944 (1995).
- [53] J. J. Mortensen, L. B. Hansen, and K. W. Jacobsen, *Phys. Rev. B* **71**, 035109 (2005).
- [54] M. Kuksma, J. Ojanen, J. Enkovaara, and T. T. Rantala, *Phys. Rev. B* **82**, 115106 (2010).
- [55] I. E. Castelli, T. Olsen, S. Datta, D. D. Landis, S. Dahl, K. S. Thygesen, and K. W. Jacobsen, *Energy Environ. Sci.* **5**, 5814 (2012).
- [56] G. Pilania, A. Mannodi-Kanakkithodi, B. Uberuaga, R. Ramprasad, J. Gubernatis, and T. Lookman, *Sci. Rep.* **6**, 19375 (2016).
- [57] A. Togo and I. Tanaka, *Scr. Mater.* **108**, 1 (2015).
- [58] A. Jain, S. Ong, G. Hautier, W. Chen, W. Richards, S. Dacek, S. Cholia, D. Gunter, D. Skinner, G. Ceder, and K. Persson, *APL Mat.* **1**, 011002 (2013).
- [59] O. Glemser and M. Filcek, *Z. Anorg. Allg. Chem.* **279**, 321 (1955).
- [60] B. A. Rosales, M. A. White, and J. Vela, *J. Am. Chem. Soc.* **140**, 3736 (2018).
- [61] S. Curtarolo, W. Setyawan, S. Wang, J. Xue, K. Yang, R. H. Taylor, L. J. Nelson, G. L. W. Hart, S. Sanvito, M. Buongiorno-Nardelli, N. Mingo, and O. Levy, *Comput. Mater. Sci.* **58**, 275 (2012).
- [62] C. Osés, E. Gossett, D. Hicks, F. Rose, M. Mehl, E. Perim, I. Takeuchi, S. Sanvito, M. Scheffler, Y. Lederer, O. Levy, C. Toher, and S. Curtarolo, *J. Chem. Inf. Model.* **58**, 2477 (2018).
- [63] W. Setyawan and S. Curtarolo, *Comput. Mater. Sci.* **49**, 299 (2010).
- [64] B. Schwedes and R. Hoppe, *Z. Anorg. Allg. Chem.* **392**, 97 (1972).
- [65] N. Kumada, N. Kinomura, P. Woodward, and A. Sleight, *J. Solid State Chem.* **116**, 281 (1995).
- [66] H. Park, F. Alharbi, S. Sanvito, N. Tabet, and F. El-Mellouhi, *ChemPhysChem* **19**, 703 (2018).
- [67] H. Park, F. H. Alharbi, S. Sanvito, N. Tabet, and F. El-Mellouhi, *J. Phys. Chem. C* **122**, 8814 (2018).
- [68] J. W. Bennett, I. Grinberg, and A. M. Rappe, *Phys. Rev. B* **79**, 235115 (2009).
- [69] M.-K. Han, Y.-S. Jin, B. Yu, W. Choi, T.-S. You, and S. Kim, *J. Mat. Chem. A* **4**, 13859 (2016).
- [70] X.-G. Zhao, G. M. Dalpian, Z. Wang, and A. Zunger, *Phys. Rev. B* **101**, 155137 (2020).
- [71] See Supplemental Material at <http://link.aps.org/supplemental/10.1103/PhysRevMaterials.4.075401> for the calculated elastic stiffness constants of the eight alkali-metal based bismuth chalcogenides, the calculated phonon spectra of NaBi₂ and KBi₂, the calculated DFT energy band structure and PDOS of KBiO₂, KBiO₃, KBiS₂, and KBiS₃, the variation in the real and imaginary parts of the dielectric function of KBiO₂, KBiO₃, NaBi₂, NaBi₃, KBi₂, and KBi₃, and the detailed information about the static dielectric tensor of the alkali-metal-based bismuth ternary chalcogenides.
- [72] S. Sanvito, C. Osés, J. Xue, A. Tiwari, M. Zic, T. Archer, P. Tozman, M. Venkatesan, J. Coey, and S. Curtarolo, *Sci. Adv.* **3**, e1602241 (2017).
- [73] C. Toher, C. Osés, D. Hicks, and S. Curtarolo, *npj Comp. Mater.* **5**, 69 (2019).

- [74] S. Ong, W. Richards, A. Jain, G. Hautier, M. Kocher, S. Cholia, D. Gunter, V. Chevrier, K. Persson, and G. Ceder, *Comput. Mater. Sci.* **68**, 314 (2013).
- [75] S. Ong, L. Wang, B. Kang, and G. Ceder, *Chem. Mater.* **20**, 1798 (2008).
- [76] S. Ong, A. Jain, G. Hautier, B. Kang, and G. Ceder, *Electrochem. Commun.* **12**, 427 (2010).
- [77] K. H. Whitmire, Bismuth: Inorganic chemistry, *Encyclopedia of Inorganic and Bioinorganic Chemistry* (American Cancer Society, 2014), pp. 1–32.
- [78] M. Born and K. Huang, *Dynamical theory of crystal lattices* (Clarendon Press, Oxford, England, 1954).
- [79] B. Karki, G. Ackland, and J. Crain, *J. Phys.: Condens. Matter* **9**, 8579 (1997).
- [80] F. Mouhat and F.-X. Coudert, *Phys. Rev. B* **90**, 224104 (2014).
- [81] Q.-J. Liu, Z.-T. Liu, and L.-P. Feng, *Phys. Status Solidi B* **248**, 1629 (2011).
- [82] N. BD, *J. Phys. Soc. Jpn.* **20**, 635 (1965).
- [83] Y.-C. Zhou, C. Zhao, F. Wang, Y.-J. Sun, L.-Y. Zheng, and X.-H. Wang, *J. Am. Ceram. Soc.* **96**, 3891 (2013).
- [84] Z.-j. Wu, E.-j. Zhao, H.-p. Xiang, X.-f. Hao, X.-j. Liu, and J. Meng, *Phys. Rev. B* **76**, 054115 (2007).
- [85] R. Hill, *Proc. Phys. Soc., Sect. A* **65**, 349 (1952).
- [86] H. Koc, A. M. Mamedov, E. Deligoz, and H. Ozisik, *arXiv:1205.3344*.
- [87] S. Chen, Y. Sun, Y.-H. Duan, B. Huang, and M.-J. Peng, *J. Alloys Compd.* **630**, 202 (2015).
- [88] S. Pugh, *Lond. Edinb. Dubl. Phil. Mag.* **45**, 823 (1954).
- [89] T. Kako, Z. Zou, M. Katagiri, and J. Ye, *Chem. Mater.* **19**, 198 (2007).
- [90] P. Umari, E. Mosconi, and F. D. Angelis, *Sci. Rep.* **4**, 4467 (2014).
- [91] J. Even, L. Pedesseau, J.-M. Jancu, and C. Katan, *J. Phys. Chem. Lett.* **4**, 2999 (2013).
- [92] S. Kang, Y. Hong, and Y. Jeon, *Bull. Korean Chem. Soc.* **35**, 1887 (2014).
- [93] C. Yang, Z. Wang, Y. Wu, Y. Lv, B. Zhou, and W.-H. Zhang, *ACS Appl. Energy Mater.* **2**, 182 (2019).
- [94] X. Lv, W. Wei, Q. Sun, F. Li, B. Huang, and Y. Dai, *Appl. Catal., B* **217**, 275 (2017).